

Probing Electrochemically Induced Structural Evolution and Oxygen Redox Reactions in Layered Lithium Iridate

Liang Li,^{*,†} Fernando C. Castro,^{||} Joong Sun Park,[‡] Haifeng Li,[⊥] Eungie Lee,[‡] Teak D. Boyko,[#] John W. Freeland,[§] Zhenpeng Yao,^{||} Timothy T. Fister,[‡] John Vinson,[¶] Eric L. Shirley,[¶] Christopher Wolverton,^{||} Jordi Cabana,[⊥] Vinayak P. Dravid,^{||} Michael M. Thackeray,[‡] and Maria K. Y. Chan^{*,†}

[†]Center for Nanoscale Materials, [‡]Chemical Sciences and Engineering Division, and [§]X-ray Science Division, Argonne National Laboratory, Argonne, Illinois 60439, United States

^{||}Department of Materials Science and Engineering, Northwestern University, Evanston, Illinois 60208, United States

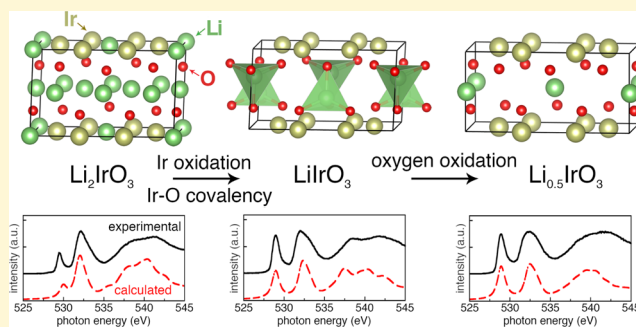
[⊥]Department of Chemistry, University of Illinois at Chicago, Chicago, Illinois 60607, United States

[#]Canadian Light Source, Saskatoon, Saskatchewan S7N 2V3, Canada

[¶]National Institute of Standards and Technology, Gaithersburg, Maryland 20899, United States

Supporting Information

ABSTRACT: In order to exploit electrochemical capacity beyond the traditionally utilized transition-metal redox reactions in lithium-metal-oxide cathode materials, it is necessary to understand the role that oxygen ions play in the charge compensation mechanisms, that is, to know the conditions triggering electron transfer on the oxygen ions and whether this transfer is correlated with battery capacity. Theoretical and experimental investigations of a model cathode material, Li-rich layered Li_2IrO_3 , have been performed to study the structural and electronic changes induced by electrochemical delithiation in a lithium-ion cell. First-principles density functional theory (DFT) calculations were used to compute the voltage profile of a $\text{Li}/\text{Li}_{2-x}\text{IrO}_3$ cell at various states of charge, and the results were in good agreement with electrochemical data. Electron energy loss spectroscopy (EELS), X-ray absorption near-edge spectroscopy (XANES), resonant/nonresonant X-ray emission spectroscopy (XES), and first-principles core-level spectra simulations using the Bethe–Salpeter Equation (BSE) approach were used to probe the change in oxygen electronic states over the $x = 0–1.5$ range. The correlated Ir M_3 -edge XANES and O K -edge XANES data provided evidence that oxygen hole states form during the early stage of delithiation at ~ 3.5 V because of the interaction between O p and Ir d states, with Ir-oxidation being the dominant source of electrochemical capacity. At higher potentials, the charge capacity was predominantly attributed to oxidation of the O^{2-} ions. It is argued that the emergence of oxygen holes alone is not necessarily indicative of electrochemical capacity beyond transition-metal oxidation because oxygen hole states can appear as a result of enhanced mixing of O p and Ir d states. Prevailing mechanisms accounting for the oxygen redox mechanism in Li-rich materials were examined by theoretical and experimental X-ray spectroscopy; however, no unambiguous spectroscopic signatures of oxygen dimer interactions or nonbonding oxygen states were identified.



1. INTRODUCTION

The widespread use of Li-ion batteries (LIBs) in portable devices is largely enabled by transition-metal (TM)-oxide cathode materials, such as LiCoO_2 .^{1,2} A growing demand for energy storage requires further performance improvements of LIBs. In this respect, considerable effort has been devoted to designing advanced cathode materials that will provide cells with higher energy density and superior cycling stability. Among the numerous cathode materials that have been explored, layered Li-rich TM oxides have been recognized as promising candidates to meet the above-stated needs.^{3–10} The

Li-rich character of these materials, designated generally as $\text{Li}_{1+x}\text{TM}_{1-x}\text{O}_2$, necessitates the existence of excess Li cations in the TM layer, which results in a higher Li/TM ratio than in an ideal layered LiTMO_2 ($x = 0$) structure such as LiCoO_2 . Beyond multivalent TM ions that are oxidized and reduced during the charge and discharge processes, respectively, when lithium is removed from, and reinserted into, the host

Received: October 31, 2018

Revised: March 22, 2019

Published: March 25, 2019

electrode structure, oxygen ions are also believed to contribute substantially to the anomalously high capacity of layered Li-rich materials.

Lithium-TM-oxide cathodes containing Ni, Mn, and Co ions, known collectively as “NMC” materials, are attractive for Li-ion battery applications because they offer higher energy storage capacities and are less expensive than LiCoO_2 , which is currently the predominant cathode material for consumer electronic devices. Luo et al.¹¹ recently investigated charge compensation mechanisms in $\text{Li}_{1.2}[\text{Ni}_{0.13}\text{Mn}_{0.54}\text{Co}_{0.13}]\text{O}_2$ electrodes during electrochemical cycling using spectroscopic techniques such as X-ray absorption near-edge spectroscopy (XANES) and resonant inelastic X-ray scattering (RIXS). They found that, besides TM oxidation, the removal of Li^+ is also charge-compensated by both irreversible oxygen evolution and the formation of holes on oxygen sites, the latter phenomenon being the dominant source of extra capacity beyond TM oxidation. A theoretical explanation of the structural and electronic origin of such an oxygen-redox-induced capacity in Li-rich and cation-disordered cathode materials has recently been proposed by Seo et al.,¹² which states that the linear Li–O–Li bonding enabled by the existence of Li atoms in the TM layers causes isolated O 2p states that are not hybridized with TM, and electrons are preferentially removed from these states once oxygen redox is activated.

Harnessing the capacity stored in the anion matrix of Li-rich metal oxide electrodes provides an intriguing route to designing novel cathode materials with extremely high capacity relative to LiCoO_2 . In addition, a deep understanding of the structural and electrochemical phenomena that occur during Li extraction/insertion reactions in these materials may enable advances in their structural design.^{13–16} Making such advances is challenging because, ultimately, the oxidation of a close-packed oxygen ion array is likely to be accompanied by oxygen loss and destabilization of the structure. For instance, it has been demonstrated that the concomitant release of O_2 during the delithiation of layered Li_2MnO_3 induces interlayer Mn migration¹⁷ and a layered-to-“spinel-like” transformation,^{18–20} making it difficult to differentiate the signal changes related to cationic/anionic redox reactions from those caused by electrochemically induced structural degradation in spectroscopic measurements. In a combined electrochemical and theoretical study, McCalla et al.⁶ demonstrated that a Li_2IrO_3 electrode, which contains a 5d TM ion and is isostructural with Li_2MnO_3 , cycles more than one Li per formula unit with reasonably good stability. Surface-sensitive X-ray photoelectron spectroscopy (XPS) was used to examine the oxygen 1s core-level state during charge, and a “peroxo-like” O–O bond was inferred from XPS peak fitting. Despite the lateral gliding of the TM layers during Li extraction, no interlayer TM cation migration was observed, and only a slight amount of released O_2 was detected above 4.3 V.⁶ Li_2IrO_3 is, therefore, a good model system to compare and understand the oxygen redox chemistry in lithium-rich TM-oxide electrode materials because of the small degree of structural degradation upon cycling. However, the detailed atomic-scale structural changes during the charge process are unclear, making the link between structural and electronic evolution elusive. Moreover, changes in the electronic properties of oxygen in the bulk of this material have not been rigorously probed, and therefore it is difficult to determine the role—or lack thereof—of oxygen redox during electrochemical cycling. Understanding the structural and electronic properties of Li_2IrO_3 at different

states of change is thus important, and it has broad implications for the family of layered TM oxide cathodes.

In this study, the structures of $\text{Li}_{2-x}\text{IrO}_3$ ($0 \leq x < 2$) and the electrochemical profile of the initial charge were investigated using a combined charge equilibration (QEeq) and density functional theory (DFT) scheme. Both the predicted structures and voltage profile show good agreement with transmission electron microscopy (TEM) and electrochemical experiments. Core-level spectroscopy was used to study the electronic structure at oxygen sites. To preclude the influence of electrolyte side reactions and measurements of solid-electrolyte interphase compounds, electron energy loss spectroscopy (EELS), X-ray emission spectroscopy (XES), and partial- and total-fluorescence-yield (PFY/TFY) mode X-ray absorption near-edge spectroscopy (XANES) were used; these techniques are attractive because of their ability to detect bulk properties and to observe directly the electronic response of oxygen to Li extraction. Previous studies proposed several mechanisms to elucidate the underlying chemical processes that trigger oxygen redox activities, based on experimental XPS,^{4,6} RIXS,^{21–23} and theoretical studies.¹² In this work, experimental and theoretical XANES and XES linked the spectroscopic signals with specific chemical processes, enabling us to examine spectroscopic signatures corresponding to the previously-proposed mechanisms. The analysis revealed significant changes in the electronic structure and emergence of oxygen hole states during the initial delithiation step. The degree of covalency between the oxygen and TM ions was found to play an important role in inducing oxygen hole states, and determining the extent to which capacity is introduced by oxygen redox reactions.

2. EXPERIMENTAL AND COMPUTATIONAL DETAILS

2.1. Synthesis. Li_2IrO_3 powder was prepared by solid-state synthesis. Stoichiometric amounts of lithium carbonate (Li_2CO_3 , 99%, Sigma-Aldrich) and iridium oxide (IrO_2 , 99%, Alfa Aesar) were thoroughly mixed with a mortar and pestle.²⁴ The precursor mixture was pressed into a pellet and fired in air at 950 °C for 2 days. The heating rate was 2 °C/min; the cooling rate was not controlled.

2.2. Electrochemistry. Electrochemical characterization was conducted with coin cells (2032 type, Hohsen) assembled in an Ar-filled box ($\text{O}_2 < 1$ ppm, $\text{H}_2\text{O} < 1$ ppm). A homogeneous slurry containing Li_2IrO_3 powder (84 wt %), carbon black (8 wt %, Super P–Li, Cabot Co.), and polyvinylidene difluoride binder (8 wt %, Solvay) was prepared with an *N*-methyl-2-pyrrolidone solvent and coated on aluminum foil. The electrode laminate was dried in a vacuum oven overnight, and electrode discs (12.7 mm diameter) were punched out for coin cell tests. The typical active material loading was 3 mg/cm². A lithium metal disc was used as the anode, and the electrolyte was 1.2 M lithium hexafluorophosphate (LiPF_6) dissolved in a 3:7 mixture solvent of ethylene carbonate and ethyl methyl carbonate. The electrochemical charge–discharge tests were conducted at 25 °C in a temperature-controlled chamber.

2.3. First-Principles DFT Calculations. DFT calculations using the plane-wave code Vienna Ab-initio Simulation Package (VASP)²⁵ with projector-augmented wave (PAW) potentials for core electrons²⁶ were performed to model the structural and thermodynamic properties of $\text{Li}_{2-x}\text{IrO}_3$. Because of the large computational load in sampling the configurational spaces of $\text{Li}_{2-x}\text{IrO}_3$, the soft version of the oxygen PAW atom potential supplied by VASP was used, in conjunction with a kinetic energy cutoff of 353 eV. To ensure the validity of utilizing soft oxygen pseudopotentials, we also computed the voltages of Li_2IrO_3 delithiation using regular oxygen pseudopotentials along with 500 eV cutoff energy, and the comparison between the soft and regular oxygen pseudopotentials results is presented in Section 3. Various types of exchange–correlation functionals and

corrections were evaluated, including the standard generalized-gradient approximation with the parametrization of Perdew–Burke–Ernzerhof (PBE),²⁷ and modified functionals with dispersion [van der Waals (vdW)] corrections. The on-site Coulomb interaction for Ir was accounted for by adding a Hubbard- U term,²⁸ with a U value of 1.0 eV adopted from a previous study.²⁹ All calculations were spin-polarized. The Brillouin-zone integration was performed using a Γ -centered grid with a k -point spacing less than 0.35 \AA^{-1} in the reciprocal space. The electronic energies near the Fermi level were smoothed using the Gaussian smearing technique with a smearing width of 0.05 eV. The lattice parameters and positions of all atoms were allowed to relax until the total-energy difference between two consecutive self-consistent iterations was less than 10^{-4} eV. All structures were relaxed twice, with the final structure from the first relaxation being used as the starting configuration for the second relaxation. All the atomic models were visualized with the VESTA package.³⁰ To obtain more accurate results on the electronic structures, the structures of $\text{Li}_{2-x}\text{IrO}_3$ on the constructed convex hull ($x = 0, 1$ and 1.5) obtained with PBE + U were further relaxed using the Heyd–Scuseria–Ernzerhof (HSE) screened hybrid functional,³¹ including spin–orbit coupling (SOC). The density of states (DOS) of these three structures were computed accordingly.

2.4. Charge Equilibration Method. The QEq approach was adopted to calculate the electrostatic energies of $\text{Li}_{2-x}\text{IrO}_3$. The methodology of QEq was introduced by Rappé and Goddard.³² In this technique, the electrostatic energy of an atom is described by its electronegativity (χ), atomic hardness (J), and covalent radius (R). The charge of an individual atom was obtained by minimizing the overall electrostatic energy of the system. It is worth noting that the electronegativity and atomic hardness of an atomic species are specific to its bonding environment and need to be explicitly determined for the Li–Ir–O system. Sen et al.²⁹ determined the QEq parameters for Ir and O by fitting to DFT-calculated energetic and structural properties of IrO_2 polymorphs. The chemical environments of Ir and O in IrO_2 and Li_2IrO_3 are similar in several ways: the valence states of Ir^{4+} and O^{2-} are identical in both compounds, and Ir atoms are octahedrally coordinated by O atoms. We thus employed the Ir and O QEq parameters from ref 29. The covalent radius of Li was also adopted from previous work,³³ and the values of χ and J for Li were determined by performing an extensive search of physically reasonable values to fit the Bader charge³⁴ of Li atoms. Details of QEq parameterization and the comparison between QEq charges and Bader charges are presented in Section S4 in the Supporting Information.

2.5. Transmission Electron Microscopy. TEM analyses were done using a JEOL 2100 FasTEM, equipped with a Schottky field-emission electron gun operating at 200 kV. This transmission electron microscope is equipped with a Gatan GIF camera system for high-resolution TEM imaging. The JEOL 2100 was also operated in scanning transmission electron microscopy (STEM) mode to conduct high-angle annular dark-field imaging, energy-dispersive X-ray spectroscopy (EDS), and EELS. Specifically, EDS analysis was collected using an Oxford Inca EDS system with a Si–Li detector. EELS were collected using a Gatan Enfina EELS spectrometer. The energy resolution for the EELS was 1.0 eV, based on the full-width half-maximum value of the EELS zero-loss peak. Furthermore, a convergence angle of 8.4 mrad and collection angle of 14 mrad were typically used in spectra acquisition. After electrochemical cycling, the cells were disassembled in a glovebox, and the active material was rinsed of electrolytes. TEM samples were prepared by scraping $\text{Li}_{2-x}\text{IrO}_3$ off the current collector and onto a copper-mesh TEM grid with a lacey carbon support film.

2.6. X-ray Absorption and Emission Spectroscopies. Ir M_{3-} edge and O K-edge X-ray absorption near edge spectroscopy (XANES) was performed for pristine and cycled samples in the electron (surface) and fluorescence (bulk) yield modes at beamline 4-ID-C of the Advanced Photon Source. Samples were transferred from a glovebox into a transfer container and then an X-ray absorption chamber in an argon environment. This was done in order to maintain a clean sample. During the measurements, the oxygen K

edge was energy-calibrated using a Sr_2RuO_4 reference measured simultaneously with the sample XAS. For the Ir M_3 edge, the energy reference was the Mo L edge. Iridium L_3 spectra were measured on cycled laminates using transmission-mode X-ray absorption spectroscopy at sector 10BM of the Advanced Photon Source. Samples were sealed using aluminized mylar to minimize oxygen and moisture exposure.

The first-charge PFY XANES and XES measurements were taken on the REIXS beamline at the Canadian Light Source (Saskatoon, Canada). The O K-edge XES spectra were collected using a Rowland circle type spectrometer with an effective resolving power of approximately 1400. The REIXS beamline resolving power for O K-edge XANES measurements is typically 5000. The samples were mounted on carbon tape inside an argon-filled glovebag before being transferred into the endstation which has a typical base pressure of 3×10^{-9} Torr. The spectra were calibrated using borosilicate glass as a reference sample. The spectra were all normalized using the drain current from a gold mesh placed upstream of the sample.

2.7. XANES Simulations. The XANES simulations were performed using the OCEAN package^{35,36} that implements the Bethe–Salpeter equation (BSE), which is built upon a DFT ground-state calculation. The ground-state charge density and the wave functions used in core-hole screening and BSE calculations were obtained using the Quantum Espresso³⁷ package. The local-density approximation was used as the exchange–correlation functional. Norm-conserving pseudopotentials from the ABINIT³⁸ distribution were used, in conjunction with a cutoff energy of 952 eV.

The size of the k -point grid used to solve the Kohn–Sham states was $6 \times 4 \times 6$ for pristine (24-atom cell) Li_2IrO_3 and was adjusted according to the size of other simulation cells. A $12 \times 9 \times 12$ k -point grid yields essentially the same result for pristine Li_2IrO_3 . The screening calculations for all the structures used a $2 \times 2 \times 2$ k -point grid. The number of unoccupied bands used for the BSE calculation was 500, and the screened core-hole potential calculation included 800 bands. It should be noted that the number of bands influences the range of energies in which the spectra are reliably simulated. When 800 and 1200 bands were used for the BSE and screening calculation, respectively, no obvious differences in the spectra were found in the energy range up to 40 eV above the edge. Only dipole-allowed transitions were considered. The photon polarization vectors were set at [100], [010], and [001], and the final spectrum of each structure was obtained by averaging the spectra generated from using each of the polarization vectors.

3. RESULTS AND DISCUSSION

3.1. Structural and Electrochemical Properties of Li_2IrO_3 . Figure 1a shows the initial voltage profiles of the Li_2IrO_3 electrode cycled between 2.0 and 4.6 V at a C/20 rate ($1\text{C} = 200 \text{ mA/g}$). The initial charge and discharge capacities are 163 and 160 mA h/g, respectively, corresponding to the (de)intercalation of ~ 1.5 Li ions per formula unit of Li_2IrO_3 . The voltage profiles exhibit two voltage plateaus at approximately 3.5 and 4.1 V. The electrochemical charge/discharge process is highly reversible, such that 83% of the initial discharge capacity was retained after 50 cycles (Figures 1b and S2). The observed electrochemical behavior of Li_2IrO_3 is consistent with that reported by McCalla et al.,⁶ who also identified the electrochemically induced structural transition between the O3-type Li_2IrO_3 and O1-type $\text{Li}_{0.5}\text{IrO}_3$ structures. Structural models of Li_2IrO_3 and $\text{Li}_{0.5}\text{IrO}_3$ are shown in Figure 1c. Pristine Li_2IrO_3 has monoclinic symmetry that belongs to the $C2/m$ space group,^{39,40} with oxygen atoms arranged in a close-packed ABC stacking sequence (O3-type), as confirmed by the Rietveld refinement of the X-ray diffraction (XRD) pattern (Figure S2). The Li atoms in the pure Li layer reside in the 2d and 4h Wyckoff positions, while in the TM layer, Li atoms are located at the 2a position. The product at the end of

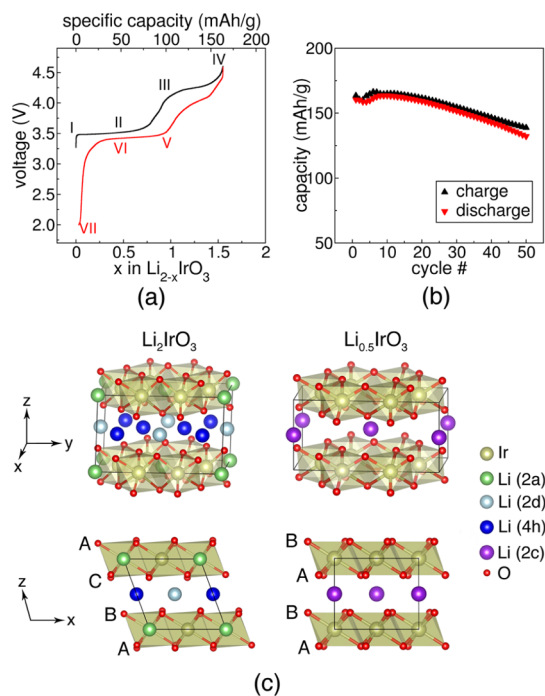


Figure 1. (a) Voltage profile of the first cycle of Li_2IrO_3 at C/20. (b) Charge/discharge capacity as a function of cycle number (first 50 cycles). (c) Structural models of Li_2IrO_3 and $\text{Li}_{0.5}\text{IrO}_3$. O stacking sequences of these two phases are labeled; Wyckoff positions of Li atoms are represented by different colors.

charge, $\text{Li}_{0.5}\text{IrO}_3$, differs from the pristine structure in several ways: the oxygen atoms are arranged in an AB sequence (O1-type) in a structure that has orthorhombic symmetry. All Li atoms initially in the TM layers are removed, while the remaining Li atoms in the pure Li layer are accommodated in the 2c Wyckoff sites, indicating intralayer migration of Li concomitant with electrochemical extraction. Such a phase transition between O3- and O1-type structures is reversible, as shown in the high-energy XRD pattern in Figure S3.

3.2. DFT-Predicted $\text{Li}_{2-x}\text{IrO}_3$ Structures. Recent theoretical studies have revealed the indispensable role of an appropriate dispersion correction when describing the structural response of layered cathode materials to Li extraction,^{41,42} with one important example being the experimentally observed interlayer spacing change of LiCoO_2 upon delithiation.⁴³ This spacing cannot be correctly reproduced by DFT calculations if vdW interactions are not considered.⁴¹ Therefore, DFT studies were initiated by first determining the appropriate vdW treatment on layered Li_2IrO_3 systems, through a thorough evaluation of the vdW-inclusive exchange–correlation functionals, in which nonlocal electron correlation effects are explicitly taken into account. As Li atoms are extracted from the system, the electrostatic interaction between layers is weakened such that dispersion effects become more dominant. Therefore, we compared the structures of Li-deficient $\text{Li}_{0.5}\text{IrO}_3$ obtained using various functionals with experimental observation. The results are presented in Section S2. The structures obtained using the optPBE-vdW⁴⁴ functional show the best overall agreement with previous experiments in terms of interlayer distance and cell volume,⁶ and therefore, this functional was adopted in the following DFT calculations.

Understanding the structural evolution induced by electrochemical Li extraction is important when elucidating the phase transitions and voltage change. We consider two theoretical approaches for predicting the stable structures during (de)intercalation. In the first, a “history-dependent” method, the Li atoms are removed in a sequential manner. The removal of each geometrically unique Li atom is performed separately, and the configuration with the lowest energy is selected as the starting configuration for the following Li removal.^{45–47} The second approach involves the enumeration of all possible Li/vacancy arrangements (or a statistical sampling thereof) at each (de)lithiation stage for a given supercell size, and evaluating the energy of each configuration using an effective Hamiltonian such as electrostatic energy,^{48,49} classical interatomic potentials⁴² or cluster expansions.^{50,51} Both approaches have proven effective for predicting the structures and voltages for different Li (de)intercalation processes. The latter, designed for on-site configurational sampling problems, was found to be more effective than history-dependent sampling (Section S3) in determining low-energy structures during the delithiation of Li_2IrO_3 .

To accelerate the configurational sampling, classical pairwise potentials⁴² or electrostatics⁴⁹ can be used to perform an initial screening of the energies of possible cationic orderings before the lowest-energy configurations are further screened by DFT calculations. To our knowledge, no classical potential parameters are available for the Li–Ir–O systems. Considering that atomic charges vary with local chemical environments, a modified electrostatics screening scheme was used in this work in which the electrostatic energies are calculated using a variable-charge approach based on QEq,³² before more accurate DFT calculations are performed using the lowest-energy structures selected by electrostatic energy ranking. This approach is similar to that adopted in previous computational work to sample nonequilibrium phases in electrochemical systems,⁵² but instead of using pre-assigned atomic charge states, the QEq method allows self-adaptive charge assignment that is responsive to the changing chemical environment.

A detailed description of the QEq parameterization and the robustness of these parameters is given in Section S4. The atomic charges calculated by the QEq approach closely match the values obtained from Bader charge analysis, and the charges of the oxygen atoms were observed to vary according to the stage of delithiation (Figure S6). All $\text{Li}_{2-x}\text{IrO}_3$ structures were generated using the derivative structures enumeration algorithm proposed by Hart and Forcade,⁵³ and the cell used in the enumeration was the conventional Li_2IrO_3 cell containing 8 Li atoms. Both O3 and O1 stacking sequences were considered for each Li content. All 2c (0.5, 0.5, 0.5), 2d (0, 0.5, 0.5), 4h (0, 0.84, 0.5), and equivalent sites in the Li layer, as well as 2a (0, 0, 0) and equivalent sites in the TM layer were considered for Li occupation. During the enumeration, a certain portion of the possible Li occupation sites were populated according to the Li concentration (value of x), with all unique combinations of occupied and unoccupied sites for the simulation cell being considered. All O3 and O1 $\text{Li}_{2-x}\text{IrO}_3$ structures were ranked by the electrostatic energy calculated using the QEq scheme. The fifteen lowest-energy configurations at each x for both O3 and O1 stacking were subsequently evaluated by DFT calculations, and the most stable structure for each x was thus obtained. Accordingly, the delithiation reaction energy ΔE_r at various delithiation stages can be calculated as

$$\Delta E_r(\text{Li}_{2-x}\text{IrO}_3) = E(\text{Li}_{2-x}\text{IrO}_3) + xE(\text{Li}) - E(\text{Li}_2\text{IrO}_3)$$

where $E(\text{Li}_{2-x}\text{IrO}_3)$, $E(\text{Li})$, and $E(\text{Li}_2\text{IrO}_3)$ represent the DFT energies of $\text{Li}_{2-x}\text{IrO}_3$, metallic Li, and pristine Li_2IrO_3 , respectively. Considering the delithiation/lithiation reaction between $\text{Li}_{x_1}\text{IrO}_3$ and $\text{Li}_{x_2}\text{IrO}_3$, where x_1 and x_2 represent adjacent stable phases on the convex hull, the equilibrium voltage (V) relative to Li/Li^+ can be computed as⁵⁴

$$V = -\{[E(\text{Li}_{x_2}\text{IrO}_3) - E(\text{Li}_{x_1}\text{IrO}_3)]/(x_2 - x_1) - E(\text{Li})\}$$

The convex hull was constructed from the formation energies obtained by both history-dependent and enumeration approaches, as shown in Figure 2a. A low-energy phase at $x = 1$

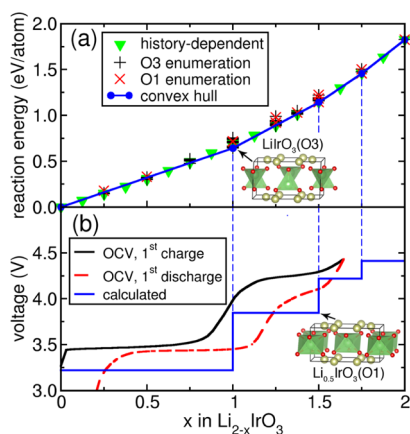


Figure 2. (a) Delithiation reaction energies of $\text{Li}_{2-x}\text{IrO}_3$ calculated using various Li-removal schemes. The reaction energies were normalized by the number of atoms in the $\text{Li}_{2-x}\text{IrO}_3$ unit cell. The convex hull was obtained using the lowest energies for each x . (b) Comparison between experimental open-circuit voltage (OCV) and calculated voltage profiles. The vertical dashed lines highlight the correspondence between the steps in the calculated voltage profile and the kinks in the reaction energy convex hull. Insets show the lowest-energy configurations sampled at $x = 1.0$ and 1.5 . Green spheres and polyhedra represent Li, yellow spheres represent Ir, and red spheres represent oxygen.

can be observed on the convex hull, which divides the calculated voltage profile into two plateaus in the $0 \leq x \leq 1.5$ interval (Figure 2b). This finding is in excellent agreement with previous measurements.^{6,55} The calculated voltages at the first and second plateaus are 3.22 and 3.85 V, respectively, which also agree reasonably well with the experimental OCV, as shown in Figure 2b. For comparison, the corresponding voltages calculated using regular oxygen pseudopotentials are 3.23 and 3.76 V, respectively. The voltages calculated using HSE functionals and different U values for the PBE + U approximation are shown in Figure S7. The structures of lowest-energy phases at $x = 1.0$ and 1.5 obtained using DFT are presented in the insets of Figure 2. In LiIrO_3 , all Li atoms reside in tetrahedral sites after DFT relaxation, rather than the original octahedral sites, while the O3 stacking is retained. In contrast, upon further Li extraction to $\text{Li}_{0.5}\text{IrO}_3$, the remaining Li atoms are more energetically likely to be in the octahedral sites, and O1 stacking becomes more stable than O3. The computed $\text{Li}_{0.5}\text{IrO}_3$ structure is identical to the experimental structure recently reported by McCalla et al.⁶ The origin of the two plateaus in the range $0 \leq x \leq 1.5$ can tentatively be attributed to the variation of the Li site energy at different

delithiation stages.⁵⁶ Figure S8 shows all the intermediate lowest-energy $\text{Li}_{2-x}\text{IrO}_3$ structures in the $0 \leq x \leq 2$ range from DFT calculations. For $0 < x \leq 1$, the Li atoms are extracted exclusively from the octahedral sites, yielding a first plateau at ~ 3.5 V. For $1 < x \leq 1.5$, Li atoms are extracted from the tetrahedral sites, which have different site energies from the octahedral sites, resulting in a second, higher voltage plateau. It is worth noting that another LiIrO_3 polymorphic structure was identified, in which all Li atoms exclusively reside in the octahedral sites between the TM layers (Figure S9a). DFT calculation shows that this structure is marginally less stable than the one with Li atoms in tetrahedral sites (Figure 2) by 56 meV/atom. Therefore, it is possible for these two structures to co-exist at elevated temperatures. Overall, DFT calculations successfully captured the phase transition of Li_2IrO_3 after 1 Li removal, and the atomic-scale morphology of the end product $\text{Li}_{0.5}\text{IrO}_3$, as observed in experiments.

3.3. Morphological Changes Observed by TEM. The phase evolution of $\text{Li}_{2-x}\text{IrO}_3$ at the nanoscale is probed through a combination of TEM imaging and diffraction. Figure 3a–f shows representative TEM images of $\text{Li}_{2-x}\text{IrO}_3$

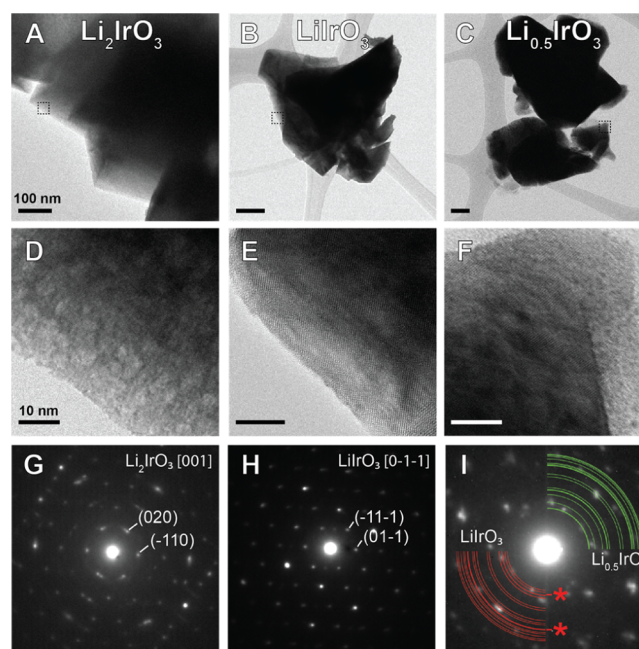


Figure 3. (a–c) Medium-magnification and (d–f) high-magnification TEM images of $\text{Li}_{2-x}\text{IrO}_3$ for (a,d) $x = 0$, (b,e) $x = 1$, and (c,f) $x = 1.5$. The $\text{Li}_{2-x}\text{IrO}_3$ samples were cycled ex situ and examined during the first delithiation cycle. Medium-magnification images have boxed regions where the high-magnification images were taken. Scale bars are 100 nm for (a–c) and 10 nm for (d–f). (g–i) Selected-area electron diffraction patterns for (g) Li_2IrO_3 , (h) LiIrO_3 , and (i) $\text{Li}_{0.5}\text{IrO}_3$. The indexed zone axes are marked in (g,h). Theoretical diffraction rings are plotted in (i) for LiIrO_3 , in red, and $\text{Li}_{0.5}\text{IrO}_3$, in green, to show the two phases. The LiIrO_3 [101] and [103] rings are marked with red asterisks.

particulates from regions I, III, and IV of the voltage profile in Figure 1a, during the first delithiation cycle. Most particles are several hundred nanometers in size but have edges that are thin enough for imaging and STEM–EELS analysis. Comparison of the $\text{Li}_{2-x}\text{IrO}_3$ images at higher magnifications (Figure 3d–f) shows no significant variation in sample morphology at the nanometer scale. This is consistent with

expectations for a Li-intercalation based material as no major changes in lattice spacings of the structure occur during delithiation.

The $\text{Li}_{2-x}\text{IrO}_3$ samples were also examined with selected area electron diffraction (SAED) in the TEM to determine the structural phase composition. Figure 3g–i exhibits representative SAED patterns of $\text{Li}_{2-x}\text{IrO}_3$ collected from regions shown in Figure 3a–c. Pristine Li_2IrO_3 was found to consist of a single phase, as expected. The SAED pattern shown in Figure 3g was indexed to the [001] zone axis. The SAED pattern was collected from two grains that were rotated with respect to each other, resulting in two sets of spots with the same zone axis but slightly different rotational orientations. LiIrO_3 , seen in Figure 3h, also demonstrated single-phase behavior and the SAED pattern could be indexed to the [0–1–1] orientation. Differentiating between $\text{Li}_{0.5}\text{IrO}_3$ and LiIrO_3 can be difficult because many of the diffraction rings for both phases have very similar d -spacings. This condition is shown in Figure 3i, which was derived with the calculated diffraction ring spacings for $\text{Li}_{0.5}\text{IrO}_3$ (green) and LiIrO_3 (red), and with the indices for all rings listed in Table S4. Some diffraction spots could not be attributed to $\text{Li}_{0.5}\text{IrO}_3$, but had d -spacings that matched with the LiIrO_3 [101] and [103] diffraction ring spacings (marked with red asterisks). It is reasonable that some residual LiIrO_3 may be present in the $\text{Li}_{0.5}\text{IrO}_3$ sample at the nanometer scale, as extraction of 1.5 Li/Ir is reached at the upper cutoff voltage for electrochemical cycling, and the delithiation reaction may not have been fully completed across the entire sample. However, the EELS data discussed later in the SI showed clear differences in both low-loss and core-loss features, and the sample could be identified as primarily $\text{Li}_{0.5}\text{IrO}_3$.

3.4. Ir-Site Electronic Structure Changes via XANES.

Oxygen redox is closely intertwined with TM redox during electrochemical processes. Changes in the Ir-oxidation state were probed by XANES of the Ir M_3 edge. Figure 4a shows the experimental Ir M_3 -edge spectra at different stages of charge, as labeled in Figure 1a; the centroid energies of the Ir M_3 edge were computed to demonstrate the change in the Ir-oxidation state (Figure 4b). On the first plateau of charge (stage I–III), the centroid energy of Ir M_3 edge increases monotonically, indicating continuous oxidation of Ir, whereas the centroid energy drops at the end of the second plateau (stage IV), which implies the reduction of Ir between stages III and IV, when the equivalent of 1.0–1.5 Li has been removed. The Ir L_3 edge shows essentially the same trend as the M_3 edge (Figure S10). A reductive coupling mechanism was proposed in previous theoretical studies,^{4,15} which states that the formation of peroxo-like O–O dimers at high voltages causes charge transfer from oxygen to highly oxidized TM, given that the peroxo-like species is covalently bound to the TM, and this would ultimately allow the TM to be reduced. However, as discussed in the following sections, O K-edge spectroscopy did not recover any spectral signatures of peroxo-like species in charged Li_2IrO_3 , so the evidence confirming the existence of oxygen dimers, or their connection to TM charge transfer, is lacking. Alternatively, it is possible that the decrease in the overall Ir-oxidation state between stages III and IV is due primarily to oxygen loss from the lattice. However, considering the good cycling stability during the first 50 cycles (Figure 1b), the loss of oxygen during each cycle appears to be minor. This was verified by the differential electrochemical mass spectrometry measurements previously reported by McCalla et al.,⁶ which showed that oxygen evolution does not occur until the

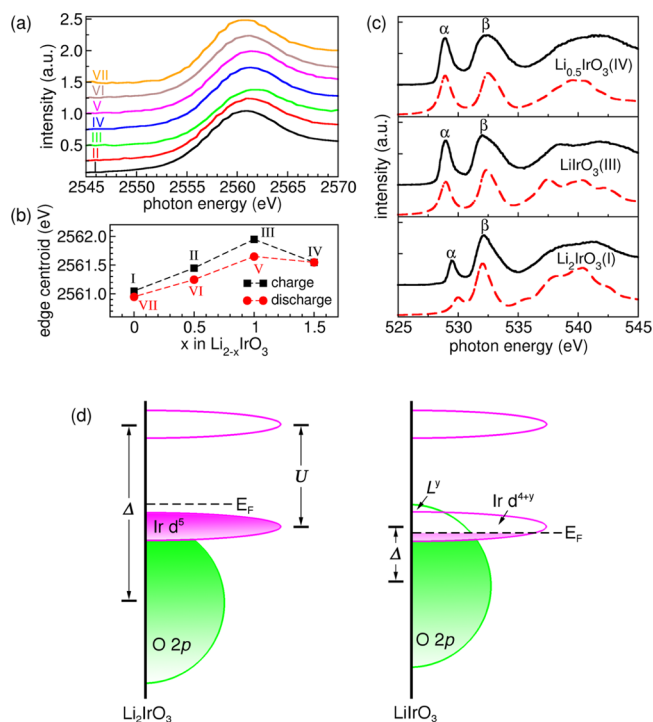


Figure 4. (a) Stack plot of experimental Ir M_3 -edge XANES and (b) Ir M_3 -edge centroid energies. (c) Experimental bulk (partial fluorescence yield) (solid black) and simulated (dashed red) O K-edge spectra. The simulated spectra are offset horizontally to align with experimental spectra and offset vertically for presentation. Spectra are collected at different stages of charge, as labeled in Figure 1a. (d) Schematic diagram of Ir 5d and O 2p states of Li_2IrO_3 and LiIrO_3 .

voltage reaches 4.3 eV, and the amount of oxygen release above 4.3 V is small. Therefore, it is unclear if such minor oxygen loss is adequate to cause the observed Ir reduction. Further studies are needed to fully understand why Ir is reduced in the second charge plateau. In the first discharge, Ir is reduced, and a reversal from the first charge can be seen, as well as substantial deviations from the charge product at $x = 0.5$ and 1.0. The oxidation state of Ir at the end of the first discharge differs slightly from that in the starting Li_2IrO_3 compound.

3.5. Oxygen-Site Electronic Structure Changes via XANES and XES. A bulk-sensitive and direct probe of the electronic structure changes in oxygen is essential for developing a comprehensive understanding of the redox reaction. Such a probe of the oxygen-site electronic structure was provided by STEM–EELS and XANES during the first charge/discharge cycle. Figure 4c shows the O K-edge XANES of $\text{Li}_{2-x}\text{IrO}_3$ ($x = 0, 1$ and 1.5) collected in the PFY mode. The BSE-simulated spectra, shown alongside the experimental results, were calculated using the DFT-derived lowest-energy structures (Figure S8). In all three structures, the broad features after 535 eV are due to the electron transition from the occupied O 1s state to the unoccupied O 2p hybridized with Ir 6sp. On the other hand, two pre-edge peaks labeled α and β correspond to the transitions to O 2p states hybridized with Ir t_{2g} and e_g d states, respectively. The computed spectra corresponding to the two different LiIrO_3 polymorphic structures (Figure S9a) were compared in Figure S9b. The two polymorphic structures result in similar spectral features in

the simulated XANES, whereas the LiIrO_3 structure with Li atoms exclusively at octahedral sites exhibits a relatively smaller splitting between α and β peaks. Experimentally, the O K-edge spectra were also collected in a surface-sensitive total-electron-yield (TEY) mode, but some of the pre-edge features are substantially different from those obtained in the fluorescence-yield mode (Figure S11). Because electron- and fluorescence-yield modes of soft X-ray absorption probe depths of a few nm⁵⁷ and ~ 100 nm,⁵⁸ respectively, such a difference can be attributed to the formation of surface phases on the electrode during electrochemical cycling,⁵⁹ highlighting the importance of using bulk-sensitive probes for determining the oxygen electronic structure.

A focal aspect of the oxygen XANES data is the evolution of the aforementioned α and β peaks during electrochemical cycling because of their sensitivity to the electronic structure of oxygen. The simulated spectra (Figure 4c) show excellent agreement with experimental measurements in terms of the changes in peak shapes and peak separations, which again corroborates the DFT-predicted structures. For the pristine Li_2IrO_3 at stage I, peaks α and β are found at 529.6 and 532.4 eV, respectively. The energy separation of 2.8 eV agrees with previously reported splitting between Ir t_{2g} and e_g states.^{40,60} Across the first charge plateau (stages II and III), peak α shifts toward lower energy, suggesting a larger splitting between Ir t_{2g} and e_g states, which, together with the increased intensity of peak α , is typically correlated with the loss of d electrons.^{61,62} Pristine Li_2IrO_3 is known to be a Mott insulator,⁴⁰ with the energy cost for moving electrons from occupied $5d$ to unoccupied $5d$ states (U) smaller than from O $2p$ to Ir $5d$ (Δ), as illustrated in Figure 4d. As the number of electrons in Ir $5d$ decreases during delithiation and the Fermi level (E_F) shifts down, the charge transfer energy Δ is reduced, which leads to a negative charge-transfer system with electrons in occupied O $2p$ transferred to unoccupied Ir $5d$, leaving self-doped holes in the O $2p$ band.^{63,64} Therefore, during the first Li removal, instead of pure TM oxidation $\text{Ir } 5d^5 \rightarrow 5d^4$, this process can be described as $5d^5 \rightarrow 5d^{4+y}L^y$ ($y > 0$), where L denotes holes in the O $2p$ band (Figure 4d). In other words, the oxygen holes arise because of enhanced mixing between O $2p$ and Ir d ; thus, the local formal charge state of Ir in LiIrO_3 is likely to be slightly lower than +5.

These results demonstrate that the oxygen holes may form by charge redistribution between O p and Ir d states at a relatively low voltage (3.5 V) and manifest themselves in the larger peak splitting and higher peak intensity in XANES measurements. However, extra capacity beyond what can be delivered by Ir^{4+} to Ir^{5+} oxidation should not be anticipated at this stage. Across the second plateau of charge (stage III to IV, starting at 4.1 V), the shape of O K-edge spectra and splitting between the two pre-edge structures are almost unchanged, indicating relatively invariant energies of the O–Ir hybridized states upon the next 0.5 Li removal. Notably, the analysis of Ir M_3 edge shows minor Ir reduction on the second charge plateau, which means that the charge capacity is not due to Ir-oxidation, and the only source of capacity at this stage is the oxidation of the oxygen lattice. To examine if this oxygen redox behavior revealed by the core-level spectra is reversible upon electrochemical cycling, oxygen K-edge XANES measurements were also performed on cycled Li_2IrO_3 and $\text{Li}_{0.5}\text{IrO}_3$. The positions and relative intensities of α and β peaks were recovered at each cycle (Figure S12), confirming the reversibility of the oxygen electronic structure evolution.

In EELS measurements, both the low-loss and core-loss regions were examined for pristine Li_2IrO_3 in addition to LiIrO_3 and $\text{Li}_{0.5}\text{IrO}_3$ samples during the first charge, and the results are shown in Section S11. By integrating the intensity of the O K-edge features in the pre-edge region, it was found that the number of unoccupied states in O $2p$ band increases as the delithiation proceeds (Figure S13), and the same trend was found in integrated XANES (not shown). The reasons for such an increase, as stated in the aforementioned discussion, are different at various delithiation stages. During the first Li removal, Ir is oxidized, and the unoccupied states on oxygen sites are due to the charge redistribution between oxygen and Ir; during the next 0.5 Li removal on the second charge plateau, considering that Ir is reduced (as evident from the Ir XANES measurements), the increase in unoccupied states in oxygen is most likely due to oxygen electron depletion that provides battery capacity.

Having concluded that the Li_2IrO_3 charge capacity above 4 eV is due to the oxidation of oxygen atoms, it is imperative to identify the chemical and electronic processes that underpin the oxygen redox activity. Sathiyaraj et al.⁴ and McCalla et al.⁶ reported that the oxygen redox in $4d$ and $5d$ TM oxides is evidenced by the shrinkage of the O–O distance from originally 2.8 Å in the pristine materials to approximately 2.5 Å at the end of charge. Such a change in the O–O distance was also observed in our DFT calculations. The interatomic distance of two oxygen atoms in the same Wyckoff position (8j and 4i) is ~ 2.5 Å in $\text{Li}_{0.5}\text{IrO}_3$ (Figure 5a). The formation of

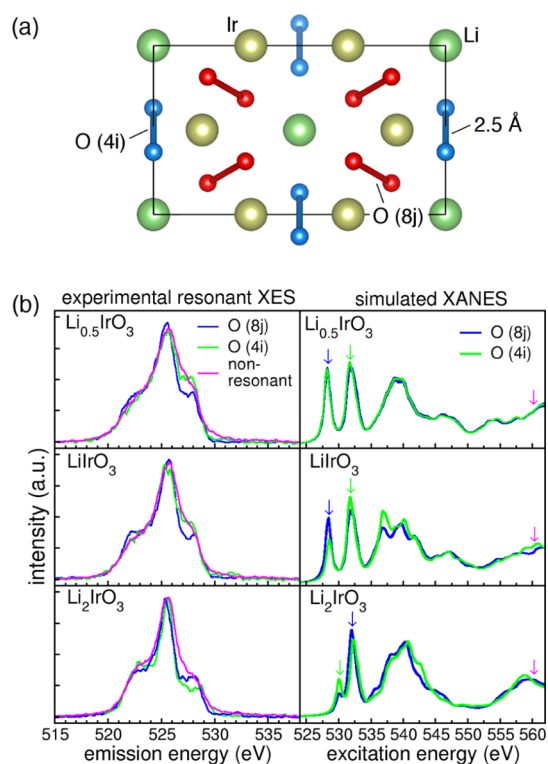


Figure 5. (a) Schematic of the 2.5 Å O–O distance in $\text{Li}_{0.5}\text{IrO}_3$. Oxygen atoms at different Wyckoff positions are represented by different colors. (b) Experimental resonant (blue and green) and nonresonant (magenta) XES (left) and simulated site-dependent oxygen K-edge XANES (right). The excitation energies of emission spectra are indicated by the arrows with corresponding colors on the right.

~ 2.5 Å oxygen bonds was corroborated by crystal orbital overlap populations (COOPs) analysis in a previous theoretical study.¹⁵ To examine if such a distance is sufficiently short to activate considerable electronic interactions between two oxygen atoms and induce O–O peroxo character that can be detected by spectroscopic experiments, the site-dependent simulated XANES are presented in Figure 5b (right). However, for all of the three compositions, both 8j and 4i oxygen atoms exhibit two absorption peaks corresponding to electron transitions from O 1s to O 2p hybridized with Ir t_{2g} and e_g states, with no additional absorption features that can be related to the O–O peroxo interaction. Therefore, based on XANES calculations, the ~ 2.5 Å bond length does not seem to induce O–O interaction.

Recently, studies have shown that some X-ray absorptions associated with particular oxygen species do not lead to distinct peaks in XANES because of the energy overlap of various absorption processes. RIXS provides an effective tool to differentiate these species by probing the occupied states of oxygen atoms.^{21–23} It is known that the O–O peroxo species is characterized by narrow energy bands below the Fermi level,⁶⁵ which is expected to be different from the broad energy band from TM–O hybridization. Therefore, to investigate the occupied states of oxygen atoms, we also performed resonant XES (RXES) experiments at specific photon energies to examine the electronic structure of different oxygen species. In the simulated XANES of Li_2IrO_3 and LiIrO_3 shown in Figure 5b, two pre-edge absorption peaks (corresponding to peaks α and β in Figure 4c) show contrasts between the nonequivalent oxygen sites (8j and 4i), while the spectral features of both 8j and 4i oxygen atoms are practically identical in $\text{Li}_{0.5}\text{IrO}_3$. Because resultant RXES depends on the relative absorption cross sections of each oxygen species, by aligning the resonant excitation energies with the two absorption peaks, the resultant Li_2IrO_3 and LiIrO_3 RXES spectra can be used to differentiate O-8j and O-4i. The left panel of Figure 5b presents the experimental results of RXES (blue and green spectra), with the resonant excitation energies indicated by the arrows in the simulated XANES on the right. Figure S14 presents the complete set of RXES results under various excitation energies, which all exhibit qualitatively the same feature as those in Figure 5b. The nonresonant XES results, with an excitation energy (560 eV) far above the resonant absorption, are also shown in Figure 5b. All the emission spectra show a peak around 525 eV, which is a universal character of TM–O hybridization that has been extensively reported.^{21–23} Several RIXS studies have reported the observation of a sharp emission feature at 523–524 eV in Li-rich layered materials at the end of charge, with an excitation energy around 531 eV.^{21–23,66} This emission peak is indicative of an oxygen electronic state that is clearly distinct from those hybridized with TM. However, such an emission feature is absent in $\text{Li}_{2-x}\text{IrO}_3$ resonant and nonresonant XES measurements (Figures 5b and S14), in which the spectra show typical TM–O hybridization characteristics throughout the first charge. Therefore, based on the site-dependent XANES and experimental XES results, we note that even though the ~ 2.5 Å O–O interaction was suggested by COOP analysis, the corresponding spectroscopic features are absent; and unlike what has been reported in $\text{Li}_{1.17}\text{Ni}_{0.21}\text{Co}_{0.08}\text{Mn}_{0.54}\text{O}_2$ and $\text{Li}_{1.2}\text{Ni}_{0.2}\text{Mn}_{0.6}\text{O}_2$,^{21–23} no sharp emission features were observed around 523–524 eV at the end of charge in Li_2IrO_3 . These analyses indicate the

absence of oxygen spectroscopic features arising outside of TM–O hybridized states in $\text{Li}_{2-x}\text{IrO}_3$.

3.6. First-Principles Electronic Analysis. DFT-derived electronic structure data were analyzed to further elucidate oxygen electronic state changes during the first charge. Figure 6a shows the projected Ir d and O p DOS for $\text{Li}_{2-x}\text{IrO}_3$,

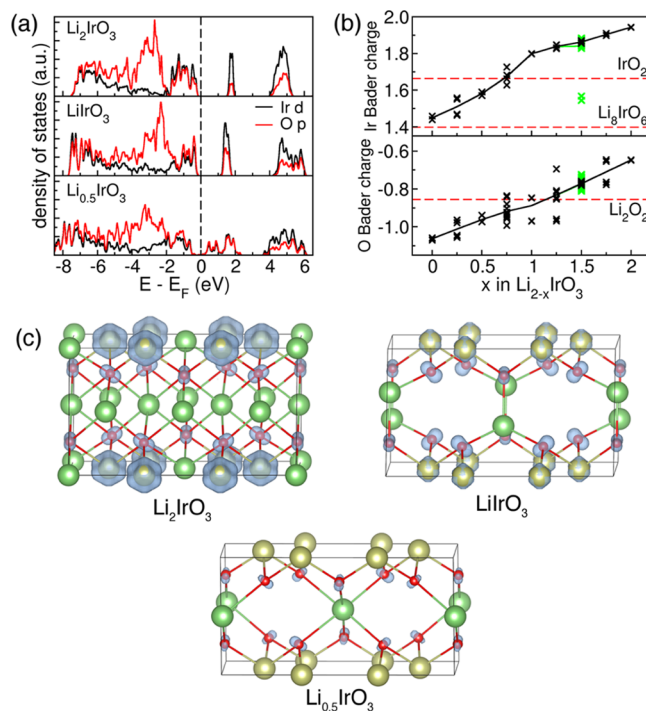


Figure 6. (a) DOS of $\text{Li}_{2-x}\text{IrO}_3$ ($x = 0, 0.5, 1$, and 1.5), calculated from DFT with the HSE functional and including SOC. Black and red lines represent the DOS of Ir d and O p states, respectively. The Fermi level is set to zero and indicated by the vertical dashed line. (b) Bader charges of Ir and O in $\text{Li}_{2-x}\text{IrO}_3$, which are computed as the difference between the valence electron numbers of neutral atoms (9 and 6 for Ir and O, respectively) and Bader population. Different points correspond to different Ir and O atoms in each structure. The green crosses indicate the Bader charges of Ir and O in 1% oxygen-deficient $\text{Li}_{0.5}\text{IrO}_3$. The lines are constructed by connecting the average Bader charges at each x . The red dashed lines indicate the Bader charges of Ir in IrO_2 and Li_3IrO_6 , and of O in Li_2O_2 , respectively. (c) Partial charge density in the energy range of -1.5 – 0 eV (blue isosurfaces) calculated for Li_2IrO_3 , LiIrO_3 , and $\text{Li}_{0.5}\text{IrO}_3$. The iso-value for the isosurfaces is 0.45 electron \AA^{-3} .

obtained using the HSE hybrid functional with SOC included. In pristine Li_2IrO_3 , the contribution of the O p states to the DOS immediately below the Fermi level is considerable, but still smaller than that of the Ir d states. The integration of DOS gives 2.32 electrons from the Ir d states, and 1.74 electrons form O p states in the region of -1.5 – 0 eV (0 eV indicates the Fermi level). As the delithiation proceeds, the O p contribution increases steadily and surpasses that of Ir d . In LiIrO_3 , the electron occupation in the Ir d states down to -1.5 eV below the Fermi level is 1.30, while in the same energy region, 1.71 electrons occupy O p states. It is worth noting that the separation between the two unoccupied bands between 0 and 6 eV above the Fermi level increases with decreasing Li content, a finding that agrees well with the increased splitting between the α and β peaks upon delithiation in Figure 4c.

The values of the Bader charge of Ir and O as a function of Li content are presented in Figure 6b. It is worth noting that even though the values of formal charges and Bader charges are different, they are generally linearly related, so that the changes in the formal charges can be reflected by Bader charge values. The formal charge state of Ir cation is +4 in pristine Li_2IrO_3 . As Li is gradually removed, Ir is oxidized and its charge state is close to +5 at $x = 1$, as mentioned in the preceding section. A kink is visible in the Ir Bader charge plot at $x = 1$, and the slope of the Bader charge versus x curve decreases at this point, which indicates the rate of Ir-oxidation per Li removed is much smaller afterward. The Ir charge state only shows a minimal change from $x = 1.0$ to $x = 1.5$ (second plateau of charge). Note that experimentally, minor oxygen loss is expected on the second plateau. The corresponding change in Ir charge states was also investigated by introducing one oxygen vacancy in a $2 \times 2 \times 2$ $\text{Li}_{0.5}\text{IrO}_3$ supercell, which translates to $\sim 1\%$ oxygen loss (for reference, the measured irreversible capacity loss per cycle is $\sim 0.34\%$). As indicated by the green crosses in Figure 6b, the presence of oxygen vacancy results in less oxidized Ir and, thus, a lower overall charge state than that of stoichiometric structures, which seems to be consistent with XANES results (Figure 4a,b). However, to achieve the Ir reduction as shown in stages III and IV in Figure 4b, a much larger amount of oxygen loss is expected, which may compromise the structural reversibility. Therefore, it is unclear whether the Ir reduction on the second charge plateau can be solely attributed to oxygen loss. In contrast, oxygen deficiency causes negligible change in the average Bader charge value of oxygen in $\text{Li}_{0.5}\text{IrO}_3$ (bottom panel, Figure 6b). It is anticipated that little to no capacity can be extracted from Ir-oxidation on the second plateau of charge. Oxygen oxidation is thus responsible for most of the capacity on the second plateau. In fact, the slope of the O Bader charge plot slightly steepens after $x = 1$, which also confirms the increased contribution from oxygen.

$\text{Li}_{2-x}\text{IrO}_3$ ($x = 0, 1$, and 1.5) partial charge densities within -1.5 – 0 eV are plotted in Figure 6c in order to differentiate the electron charge densities associated with Ir and O below the Fermi level. In Li_2IrO_3 , this energy range includes both Ir and O states, as suggested by the blue isosurfaces surrounding Ir and O atoms. Particularly, a nonbonding O $2p$ state due to the Li–O–Li bonds in Li-rich materials was suggested as the source of reversible oxygen capacity,^{11,12,67} and the visualized charge density of oxygen also has a directional distribution that aligns with the Li–O–Li direction. After one Li removal, in LiIrO_3 , Ir charge density is tremendously reduced, while oxygen charge density does not show much change compared with Li_2IrO_3 . After the subsequent 0.5 Li removal, in $\text{Li}_{0.5}\text{IrO}_3$, the partial charge density around oxygen is greatly decreased, which implies that electrons are depleted from oxygen on the second charge plateau. Figure 6c indicates that the oxygen electron depletion during LiIrO_3 to $\text{Li}_{0.5}\text{IrO}_3$ transition exclusively occurs in the states along the Li–O–Li direction. This seems to be consistent with the description of the nonbonding O $2p$ state in a previous theoretical study.¹² Electron removal from such a nonbonding state is expected to lead to unoccupied states right above the Fermi level, which causes X-ray absorption features that are likely to be found at the onset of absorption. However, this feature may be weak or partly overlap with peak α . The absorption associated with the nonbonding O $2p$ states along the Li–O–Li direction is therefore not conclusive based on the current core-level

spectroscopic measurements, and it needs to be validated by further experimental and theoretical investigations.

4. CONCLUSIONS

Low-energy $\text{Li}_{2-x}\text{IrO}_3$ ($0 \leq x < 2$) structures have been predicted by DFT calculations in combination with electrostatic prescreening using QEq, an approach that can be applied to other electrochemical systems. The experimental voltage profile of a Li/ $\text{Li}_{2-x}\text{IrO}_3$ cell and XANES data of the $\text{Li}_{2-x}\text{IrO}_3$ electrode validated, respectively, the predicted profile and structures. EELS and XANES measurements, in conjunction with first-principles spectra simulations and DFT calculations, indicated that in the early stage of charge (first charge plateau, $0 < x \leq 1$), the generation of oxygen hole states is associated with the oxidation of the Ir ions concurrent with an increased hybridization between O p and Ir d states. In the later stage of charge (second charge plateau, $1 < x \leq 1.5$), formation of oxygen hole states independent of TM–O hybridization accounts for the increase in Li_2IrO_3 specific capacity beyond the oxidation of Ir^{4+} to Ir^{5+} . Although the O K-edge XANES spectra show drastic changes during the early stage of delithiation, additional capacity beyond Ir-oxidation is not anticipated at this stage. At higher voltages (above 4 V), oxygen is oxidized without significant O_2 release, contributing $0.5 e^-$ at each cycle, which accounts for 1/3 of the total capacity. Prevailing mechanisms accounting for the oxygen redox mechanism in Li-rich materials were examined by theoretical and experimental XANES and RXES; however, no unambiguous spectroscopic signatures of O–O interaction or nonbonding oxygen states were identified. The results of this study show that the combination of first-principles computation and core-level spectroscopy provides an effective tool to identify the electronic details of chemical reactions and have implications for understanding and characterizing alternative materials in the search for high-capacity cathode systems that operate by reversible cationic/anionic redox reactions.

■ ASSOCIATED CONTENT

Supporting Information

The Supporting Information is available free of charge on the ACS Publications website at DOI: 10.1021/acs.chemmater.8b04591.

In situ XRD patterns of $\text{Li}_{2-x}\text{IrO}_3$, comparison between vdW-inclusive functionals, history-dependent Li removal of Li_2IrO_3 , QEq parameterization, DFT-predicted $\text{Li}_{2-x}\text{IrO}_3$ structures, indices for rings listed in Figure 3i, experimental Ir L_3 -edge XANES, total electron yield (TEY) O K-edge XANES, XANES measurements on cycled samples, and EELS and RXES results (PDF)

■ AUTHOR INFORMATION

Corresponding Authors

*E-mail: liangli@anl.gov (L.L.).

*E-mail: mchan@anl.gov (M.K.Y.C.).

ORCID

Liang Li: 0000-0002-6739-5022

Zhenpeng Yao: 0000-0001-8286-8257

Timothy T. Fister: 0000-0001-6537-6170

John Vinson: 0000-0002-7619-7060

Christopher Wolverton: 0000-0003-2248-474X

Jordi Cabana: 0000-0002-2353-5986

Vinayak P. Dravid: 0000-0002-6007-3063

Maria K. Y. Chan: 0000-0003-0922-1363

Notes

The authors declare no competing financial interest.

ACKNOWLEDGMENTS

This work was supported as a part of the Center for Electrochemical Energy Science, an Energy Frontier Research Center funded by the US Department of Energy, Office of Science, Basic Energy Sciences under award number DE-AC02-06CH11. Use of the Center for Nanoscale Materials and the Advanced Photon Source, both Office of Science user facilities operated by Argonne National Laboratory, was supported by the U.S. Department of Energy, Office of Science, Office of Basic Energy Sciences, under Contract No. DE-AC02-06CH11357. This work made use of the EPIC facility of Northwestern University's NUANCE Center, which has received support from the Soft and Hybrid Nanotechnology Experimental (SHyNE) Resource (NSF ECCS-1542205); the MRSEC program (NSF DMR-1720139) at the Materials Research Center; the International Institute for Nanotechnology (IIN); the Keck Foundation; and the State of Illinois, through the IIN. J.C. and H.L. acknowledge support by the National Science Foundation under Grant No. DMR-1809372. PFY XANES and XES measurements were performed at the Canadian Light Source, which is supported by the Canada Foundation for Innovation, Natural Sciences and Engineering Research Council of Canada, the University of Saskatchewan, the Government of Saskatchewan, Western Economic Diversification Canada, the National Research Council Canada, and the Canadian Institutes of Health Research. XANES simulations were performed using the National Energy Research Scientific Computing Center (NERSC), a DOE Office of Science User Facility supported by the Office of Science of the U.S. Department of Energy (DOE) under Contract No. DE-AC02-05CH11231. The computing resources provided on Blues, a high-performance computing cluster operated by the Laboratory Computing Resource Center at Argonne National Laboratory, is also gratefully acknowledged, as is the Extreme Science and Engineering Discovery Environment (XSEDE), supported by National Science Foundation grant number ACI-1053575.⁶⁸

REFERENCES

- (1) Mizushima, K.; Jones, P. C.; Wiseman, P. J.; Goodenough, J. B. Li_xCoO_2 ($0 < x < 1$): A new cathode material for batteries of high energy density. *Mater. Res. Bull.* **1980**, *15*, 783–789.
- (2) Whittingham, M. S. Lithium Batteries and Cathode Materials. *Chem. Rev.* **2004**, *104*, 4271–4302.
- (3) Robertson, A. D.; Bruce, P. G. Mechanism of Electrochemical Activity in Li_2MnO_3 . *Chem. Mater.* **2003**, *15*, 1984–1992.
- (4) Sathiyaraj, M.; Rousse, G.; Ramesha, K.; Laisa, C. P.; Vezin, H.; Sougrati, M. T.; Doublet, M.-L.; Foix, D.; Gonbeau, D.; Walker, W.; et al. Reversible Anionic Redox Chemistry in High-Capacity Layered-Oxide Electrodes. *Nat. Mater.* **2013**, *12*, 827–835.
- (5) Sathiyaraj, M.; Abakumov, A. M.; Foix, D.; Rousse, G.; Ramesha, K.; Saubanère, M.; Doublet, M. L.; Vezin, H.; Laisa, C. P.; Prakash, A. S.; et al. Origin of Voltage Decay in High-Capacity Layered Oxide Electrodes. *Nat. Mater.* **2015**, *14*, 230–238.
- (6) McCalla, E.; Abakumov, A. M.; Saubanère, M.; Foix, D.; Berg, E. J.; Rousse, G.; Doublet, M.-L.; Gonbeau, D.; Novak, P.; Van Tendeloo, G.; et al. Visualization of O-O Peroxo-like Dimers in High-Capacity Layered Oxides for Li-Ion Batteries. *Science* **2015**, *350*, 1516–1521.

- (7) Li, B.; Shao, R.; Yan, H.; An, L.; Zhang, B.; Wei, H.; Ma, J.; Xia, D.; Han, X. Understanding the Stability for Li-Rich Layered Oxide Li_2RuO_3 Cathode. *Adv. Funct. Mater.* **2016**, *26*, 1330–1337.

- (8) Wang, J.; He, X.; Paillard, E.; Laszczynski, N.; Li, J.; Passerini, S. Lithium- and Manganese-Rich Oxide Cathode Materials for High-Energy Lithium Ion Batteries. *Adv. Energy Mater.* **2016**, *6*, 1600906.

- (9) Thackeray, M. M.; Kang, S.-H.; Johnson, C. S.; Vaughey, J. T.; Benedek, R.; Hackney, S. A. Li_2MnO_3 -Stabilized LiMO_2 (M = Mn, Ni, Co) Electrodes for Lithium-Ion Batteries. *J. Mater. Chem.* **2007**, *17*, 3112–3125.

- (10) Lu, Z.; Beaulieu, L. Y.; Donaberger, R. A.; Thomas, C. L.; Dahn, J. R. Synthesis, Structure, and Electrochemical Behavior of $\text{Li}[\text{Ni}_x\text{Li}_{1/3-2x/3}\text{Mn}_{2/3-x/3}]\text{O}_2$. *J. Electrochem. Soc.* **2002**, *149*, A778.

- (11) Luo, K.; Roberts, M. R.; Hao, R.; Guerrini, N.; Pickup, D. M.; Liu, Y.-S.; Edström, K.; Guo, J.; Chadwick, A. V.; Duda, L. C.; et al. Charge-Compensation in 3d-Transition-Metal-Oxide Intercalation Cathodes through the Generation of Localized Electron Holes on Oxygen. *Nat. Chem.* **2016**, *8*, 684–691.

- (12) Seo, D.-H.; Lee, J.; Urban, A.; Malik, R.; Kang, S.; Ceder, G. The Structural and Chemical Origin of the Oxygen Redox Activity in Layered and Cation-Disordered Li-Excess Cathode Materials. *Nat. Chem.* **2016**, *8*, 692–697.

- (13) Freire, M.; Kosova, N. V.; Jordy, C.; Chateigner, D.; Lebedev, O. I.; Maignan, A.; Pralong, V. A New Active Li–Mn–O Compound for High Energy Density Li-Ion Batteries. *Nat. Mater.* **2016**, *15*, 173–177.

- (14) Grimaud, A.; Hong, W. T.; Shao-Horn, Y.; Tarascon, J.-M. Anionic Redox Processes for Electrochemical Devices. *Nat. Mater.* **2016**, *15*, 121–126.

- (15) Saubanère, M.; McCalla, E.; Tarascon, J.-M.; Doublet, M.-L. The Intriguing Question of Anionic Redox in High-Energy Density Cathodes for Li-Ion Batteries. *Energy Environ. Sci.* **2016**, *9*, 984–991.

- (16) Xie, Y.; Saubanère, M.; Doublet, M.-L. Requirements for Reversible Extra-Capacity in High Energy Density Materials for Li-Ion Batteries. *Energy Environ. Sci.* **2017**, *10*, 266–274.

- (17) Wang, R.; He, X.; He, L.; Wang, F.; Xiao, R.; Gu, L.; Li, H.; Chen, L. Atomic Structure of Li_2MnO_3 after Partial Delithiation and Re-Lithiation. *Adv. Energy Mater.* **2013**, *3*, 1358–1367.

- (18) Rana, J.; Stan, M.; Kloepsch, R.; Li, J.; Schumacher, G.; Welter, E.; Zizak, I.; Banhart, J.; Winter, M. Structural Changes in Li_2MnO_3 Cathode Material for Li-Ion Batteries. *Adv. Energy Mater.* **2014**, *4*, 1300998.

- (19) Lee, E.; Persson, K. A. Structural and Chemical Evolution of the Layered Li-Excess Li_xMnO_3 as a Function of Li Content from First-Principles Calculations. *Adv. Energy Mater.* **2014**, *4*, 1400498.

- (20) Johnson, C. S.; Li, N.; Vaughey, J. T.; Hackney, S. A.; Thackeray, M. M. Lithium–Manganese Oxide Electrodes with Layered–Spinel Composite Structures $x\text{Li}_2\text{MnO}_3 \cdot (1-x)\text{Li}_{1+y}\text{Mn}_{2-y}\text{O}_4$ ($0 < x < 1$, $0 \leq y \leq 0.33$) for Lithium Batteries. *Electrochem. Commun.* **2005**, *7*, 528–536.

- (21) Yang, W.; Devereaux, T. P. Anionic and Cationic Redox and Interfaces in Batteries: Advances from Soft X-Ray Absorption Spectroscopy to Resonant Inelastic Scattering. *J. Power Sources* **2018**, *389*, 188–197.

- (22) Gent, W. E.; Lim, K.; Liang, Y.; Li, Q.; Barnes, T.; Ahn, S.; Stone, K. H.; McIntire, M.; Hong, J.; Song, J. H.; et al. Coupling between Oxygen Redox and Cation Migration Explains Unusual Electrochemistry in Lithium-Rich Layered Oxides. *Nat. Commun.* **2017**, *8*, 2091.

- (23) Xu, J.; Sun, M.; Qiao, R.; Renfrew, S. E.; Ma, L.; Wu, T.; Hwang, S.; Nordlund, D.; Su, D.; Amine, K.; et al. Elucidating Anionic Oxygen Activity in Lithium-Rich Layered Oxides. *Nat. Commun.* **2018**, *9*, 947.

- (24) Identification of a commercial product is for purposes of clarity and should not be considered as an endorsement.

- (25) Kresse, G.; Furthmüller, J. Efficient Iterative Schemes for Ab Initio Total-Energy Calculations Using a Plane-Wave Basis Set. *Phys. Rev. B: Condens. Matter Mater. Phys.* **1996**, *54*, 11169–11186.

- (26) Kresse, G.; Joubert, D. From Ultrasoft Pseudopotentials to the Projector Augmented-Wave Method. *Phys. Rev. B: Condens. Matter Mater. Phys.* **1999**, *59*, 1758–1775.
- (27) Perdew, J. P.; Burke, K.; Ernzerhof, M. Generalized Gradient Approximation Made Simple. *Phys. Rev. Lett.* **1996**, *77*, 3865.
- (28) Dudarev, S. L.; Botton, G. A.; Savrasov, S. Y.; Humphreys, C. J.; Sutton, A. P. Electron-Energy-Loss Spectra and the Structural Stability of Nickel Oxide: An LSDA+U Study. *Phys. Rev. B: Condens. Matter Mater. Phys.* **1998**, *57*, 1505–1509.
- (29) Sen, F. G.; Kinaci, A.; Narayanan, B.; Gray, S. K.; Davis, M. J.; Sankaranarayanan, S. K. R. S.; Chan, M. K. Y. Towards Accurate Prediction of Catalytic Activity in IrO₂ Nanoclusters via First Principles-Based Variable Charge Force Field. *J. Mater. Chem. A* **2015**, *3*, 18970–18982.
- (30) Momma, K.; Izumi, F. VESTA 3 for Three-Dimensional Visualization of Crystal, Volumetric and Morphology Data. *J. Appl. Crystallogr.* **2011**, *44*, 1272–1276.
- (31) Heyd, J.; Scuseria, G. E.; Ernzerhof, M. Hybrid Functionals Based on a Screened Coulomb Potential. *J. Chem. Phys.* **2003**, *118*, 8207–8215.
- (32) Rappé, A. K.; Goddard, W. A., III Charge Equilibration for Molecular Dynamics Simulations. *J. Phys. Chem.* **1991**, *95*, 3358–3363.
- (33) Cordero, B.; Gómez, V.; Platero-Prats, A. E.; Revés, M.; Echeverría, J.; Cremades, E.; Barragán, F.; Alvarez, S. Covalent Radii Revisited. *Dalton Trans.* **2008**, 2832–2838.
- (34) Tang, W.; Sanville, E.; Henkelman, G. A Grid-Based Bader Analysis Algorithm without Lattice Bias. *J. Phys.: Condens. Matter* **2009**, *21*, 084204.
- (35) Vinson, J.; Rehr, J. J.; Kas, J. J.; Shirley, E. L. Bethe-Salpeter Equation Calculations of Core Excitation Spectra. *Phys. Rev. B: Condens. Matter Mater. Phys.* **2011**, *83*, 115106.
- (36) Gilmore, K.; Vinson, J.; Shirley, E. L.; Prendergast, D.; Pemmaraju, C. D.; Kas, J. J.; Vila, F. D.; Rehr, J. J. Efficient Implementation of Core-Excitation Bethe-Salpeter Equation Calculations. *Comput. Phys. Commun.* **2015**, *197*, 109–117.
- (37) Giannozzi, P.; Baroni, S.; Bonini, N.; Calandra, M.; Car, R.; Cavazzoni, C.; Ceresoli, D.; Chiarotti, G. L.; Cococcioni, M.; Dabo, I.; et al. QUANTUM ESPRESSO: A Modular and Open-Source Software Project for Quantum Simulations of Materials. *J. Phys.: Condens. Matter* **2009**, *21*, 395502.
- (38) Gonze, X.; Beuken, J.-M.; Caracas, R.; Detraux, F.; Fuchs, M.; Rignanese, G.-M.; Sindic, L.; Verstraete, M.; Zerah, G.; Jollet, F.; et al. First-Principles Computation of Material Properties: The ABINIT Software Project. *Comput. Mater. Sci.* **2002**, *25*, 478–492.
- (39) O'Malley, M. J.; Verweij, H.; Woodward, P. M. Structure and Properties of Ordered Li₂IrO₃ and Li₂PtO₃. *J. Solid State Chem.* **2008**, *181*, 1803–1809.
- (40) Gretarsson, H.; Clancy, J. P.; Liu, X.; Hill, J. P.; Bozin, E.; Singh, Y.; Manni, S.; Gegenwart, P.; Kim, J.; Said, A. H.; et al. Crystal-Field Splitting and Correlation Effect on the Electronic Structure of A₂IrO₃. *Phys. Rev. Lett.* **2013**, *110*, 076402.
- (41) Aykol, M.; Kim, S.; Wolverton, C. Waals Interactions in Layered Lithium Cobalt Oxides. *J. Phys. Chem. C* **2015**, *119*, 19053–19058.
- (42) Dixit, M.; Kosa, M.; Lavi, O. S.; Markovsky, B.; Aurbach, D.; Major, D. T. Thermodynamic and Kinetic Studies of Li-Ni_{0.5}Co_{0.2}Mn_{0.3}O₂ as a Positive Electrode Material for Li-Ion Batteries Using First Principles. *Phys. Chem. Chem. Phys.* **2016**, *18*, 6799–6812.
- (43) Amatucci, G. G.; Tarascon, J. M.; Klein, L. C. The End Member of the Li_xCoO₂ Solid Solution. *J. Electrochem. Soc.* **1996**, *143*, 1114–1123.
- (44) Klime, J.; Bowler, D. R.; Michaelides, A. Van Der Waals Density Functionals Applied to Solids. *Phys. Rev. B: Condens. Matter Mater. Phys.* **2011**, *83*, 195131.
- (45) Chevrier, V. L.; Dahn, J. R. First Principles Model of Amorphous Silicon Lithiation. *J. Electrochem. Soc.* **2009**, *156*, A454–A458.
- (46) Chan, M. K. Y.; Wolverton, C.; Greeley, J. P. First Principles Simulations of the Electrochemical Lithiation and Delithiation of Faceted Crystalline Silicon. *J. Am. Chem. Soc.* **2012**, *134*, 14362–14374.
- (47) Lim, Y.-G.; Kim, D.; Lim, J.-M.; Kim, J.-S.; Yu, J.-S.; Kim, Y.-J.; Byun, D.; Cho, M.; Cho, K.; Park, M.-S. Anti-fluorite Li₆CoO₄ as an alternative lithium source for lithium ion capacitors: an experimental and first principles study. *J. Mater. Chem. A* **2015**, *3*, 12377–12385.
- (48) Hautier, G.; Fischer, C. C.; Jain, A.; Mueller, T.; Ceder, G. Finding Nature's Missing Ternary Oxide Compounds Using Machine Learning and Density Functional Theory. *Chem. Mater.* **2010**, *22*, 3762–3767.
- (49) He, K.; Yao, Z.; Hwang, S.; Li, N.; Sun, K.; Gan, H.; Du, Y.; Zhang, H.; Wolverton, C.; Su, D. Kinetically-Driven Phase Transformation during Lithiation in Copper Sulfide Nanoflakes. *Nano Lett.* **2017**, *17*, 5726–5733.
- (50) Chen, W.; Schmidt, D.; Schneider, W. F.; Wolverton, C. First-Principles Cluster Expansion Study of Missing-Row Reconstructions of fcc (110) Surfaces. *Phys. Rev. B: Condens. Matter Mater. Phys.* **2011**, *83*, 075415.
- (51) Van der Ven, A.; Ceder, G. Vacancies in Ordered and Disordered Binary Alloys Treated with the Cluster Expansion. *Phys. Rev. B: Condens. Matter Mater. Phys.* **2005**, *71*, 054102.
- (52) Yao, Z.; Kim, S.; Aykol, M.; Li, Q.; Wu, J.; He, J.; Wolverton, C. Revealing the Conversion Mechanism of Transition Metal Oxide Electrodes during Lithiation from First-Principles. *Chem. Mater.* **2017**, *29*, 9011–9022.
- (53) Hart, G. L. W.; Forcade, R. W. Algorithm for Generating Derivative Structures. *Phys. Rev. B: Condens. Matter Mater. Phys.* **2008**, *77*, 224115.
- (54) Aydinol, M. K.; Kohan, A. F.; Ceder, G.; Cho, K.; Joannopoulos, J. Ab initio study of lithium intercalation in metal oxides and metal dichalcogenides. *Phys. Rev. B: Condens. Matter Mater. Phys.* **1997**, *56*, 1354–1365.
- (55) Kobayashi, H.; Tabuchi, M.; Shikano, M.; Kageyama, H.; Kanno, R. Structure, and magnetic and electrochemical properties of layered oxides, Li₂IrO₃. *J. Mater. Chem.* **2003**, *13*, 957–962.
- (56) Liu, C.; Neale, Z. G.; Cao, G. Understanding Electrochemical Potentials of Cathode Materials in Rechargeable Batteries. *Mater. Today* **2016**, *19*, 109–123.
- (57) Abbate, M.; Goedkoop, J. B.; de Groot, F. M. F.; Grioni, M.; Fuggle, J. C.; Hofmann, S.; Petersen, H.; Sacchi, M. Probing Depth of Soft X-Ray Absorption Spectroscopy Measured in Total-Electron-Yield Mode. *Surf. Interface Anal.* **1992**, *18*, 65–69.
- (58) Asakura, D.; Hosono, E.; Nanba, Y.; Zhou, H.; Okabayashi, J.; Ban, C.; Glans, P.-A.; Guo, J.; Mizokawa, T.; Chen, G.; et al. Material/Element-Dependent Fluorescence-Yield Modes on Soft X-Ray Absorption Spectroscopy of Cathode Materials for Li-Ion Batteries. *AIP Adv.* **2016**, *6*, 035105.
- (59) Fister, T. T.; Schmidt, M.; Fenter, P.; Johnson, C. S.; Slater, M. D.; Chan, M. K. Y.; Shirley, E. L. Electronic Structure of Lithium Battery Interphase Compounds: Comparison between Inelastic x-Ray Scattering Measurements and Theory. *J. Chem. Phys.* **2011**, *135*, 224513.
- (60) Sohn, C. H.; Kim, H.-S.; Qi, T. F.; Jeong, D. W.; Park, H. J.; Yoo, H. K.; Kim, H. H.; Kim, J.-Y.; Kang, T. D.; Cho, D.-Y.; et al. Mixing between J_{eff} = 1/2 and 3/2 Orbitals in Na₂IrO₃: A Spectroscopic and Density Functional Calculation Study. *Phys. Rev. B: Condens. Matter Mater. Phys.* **2013**, *88*, 085125.
- (61) Yoshiya, M.; Tanaka, I.; Kaneko, K.; Adachi, H. First principles calculation of chemical shifts in ELNES/NEXAFS of titanium oxides. *J. Phys.: Condens. Matter* **1999**, *11*, 3217–3228.
- (62) Park, J.-H.; Chen, C. T.; Cheong, S.-W.; Bao, W.; Meigs, G.; Chakarian, V.; Idzerda, Y. U. Electronic Aspects of the Ferromagnetic Transition in Manganese Perovskites. *Phys. Rev. Lett.* **1996**, *76*, 4215–4218.
- (63) Zaanen, J.; Sawatzky, G. A.; Allen, J. W. Band Gaps and Electronic Structure of Transition-Metal Compounds. *Phys. Rev. Lett.* **1985**, *55*, 418–421.

(64) Bisogni, V.; Catalano, S.; Green, R. J.; Gibert, M.; Scherwitzl, R.; Huang, Y.; Strocov, V. N.; Zubko, P.; Balandeh, S.; Triscone, J.; et al. Ground State Oxygen Holes and the Metal-Insulator Transition in the Negative Charge Transfer Rare-Earth Nickelates. *Nat. Commun.* **2016**, *7*, 13017.

(65) Streltsov, S. S.; Shorikov, A. O.; Skornyakov, S. L.; Poteryaev, A. I.; Khomskii, D. I. Unexpected 3+ Valence of Iron in FeO₂, a Geologically Important Material Lying “in between” Oxides and Peroxides. *Sci. Rep.* **2017**, *7*, 13005.

(66) Luo, K.; Roberts, M. R.; Guerrini, N.; Tapia-Ruiz, N.; Hao, R.; Massel, F.; Pickup, D. M.; Ramos, S.; Liu, Y.-S.; Guo, J.; et al. Anion Redox Chemistry in the Cobalt Free 3d Transition Metal Oxide Intercalation Electrode Li[Li_{0.2}Ni_{0.2}Mn_{0.6}]O₂. *J. Am. Chem. Soc.* **2016**, *138*, 11211–11218.

(67) Zhan, C.; Yao, Z.; Lu, J.; Ma, L.; Maroni, V. A.; Li, L.; Lee, E.; Alp, E. E.; Wu, T.; Wen, J.; et al. Enabling the High Capacity of Lithium-Rich Anti-Fluorite Lithium Iron Oxide by Simultaneous Anionic and Cationic Redox. *Nat. Energy* **2017**, *2*, 963–971.

(68) Towns, J.; Cockerill, T.; Dahan, M.; Foster, I.; Gaither, K.; Grimshaw, A.; Hazlewood, V.; Lathrop, S.; Lifka, D.; Peterson, G. D.; et al. XSEDE: Accelerating Scientific Discovery. *Comput. Sci. Eng.* **2014**, *16*, 62–74.